Atmospheric Corrosion of Mg Alloy AZ91D Fabricated by a Semi-Solid Casting Technique: The Influence of Microstructure

Citation for the original published paper (version of record):
Esmaily, M., Mortazavi Seyedeh, N., Svensson, J. et al (2015). Atmospheric Corrosion of Mg Alloy AZ91D Fabricated by a Semi-Solid Casting Technique: The
Influence of Microstructure. Journal of the Electrochemical Society, 162(7): C311-C321.
http://dx.doi.org/10.1149/2.0341507jes

Atmospheric Corrosion of Mg Alloy AZ91D Fabricated by a Semi-Solid Casting Technique: The Influence of Microstructure

M. Esmaily,[a,*,z] N. Mortazavi,[b,*] J. E. Svensson,[a,] M. Halvarsson,[b] D. B. Blücher,[c] A. E. W. Jarfors,[d] M. Wessén,[d] and L. G. Johansson[a]**

[a]*Department of Chemical and Biological Engineering, Chalmers University of Technology, SE-412 96 Göteborg, Sweden*
[b]*Department of Applied Physics, Chalmers University of Technology, SE-412 96 Göteborg, Sweden*
[c]*SINTEF Materials and Chemistry, N-7465 Trondheim, Norway*
[d]*Department of Materials and Manufacturing - Casting, Jönköping University, SE-551 11 Jönköping, Sweden*

The atmospheric corrosion behavior of alloy AZ91D produced by a semi-solid metal (SSM) technique and by conventional high pressure die casting (HPDC) was investigated for up to 1176 hours in the laboratory. Alloy AZ91D in the SSM state was fabricated using a rheocasting (RC) technique in which the slurry was prepared by the RheoMetal process. Exposures were performed in 95% RH air at 22 and 4°C. The RC alloy AZ91D exhibited significantly better corrosion resistance than the HPDC material at two temperatures studied. The effect of casting technology on corrosion is explained in terms of the microstructural differences between the materials. For example, the larger number density of cathodic β phase particles in the HPDC material initially causes relatively rapid corrosion compared to the RC material. During later stages of corrosion, the more network-like β phase particles in the RC alloy act as a corrosion barrier, further improving the relative corrosion resistance of the RC material.
 [DOI: 10.1149/2.0341507jes]

Manuscript submitted February 24, 2015; revised manuscript received March 24, 2015. Published April 1, 2015.

Conventional magnesium-aluminum (Mg-Al) alloys, i.e., AZ91D, AM50A and AM60B, offer an exceptional combination of ambient temperature strength and ductility, and good die-castability.[1–4] Cast components made of Mg-Al alloys are usually cast by conventional high pressure die casting (HPDC). Despite its advantages over many other casting techniques for producing cast Mg-Al components, there are some inherent problems associated with HPDC. For example, there is a tendency for hot tearing during HPDC due to a relatively wide freezing range and a low solidus temperature. Also, a relatively high fraction of trapped air porosity may form during the turbulent die filling, especially in thick-walled components. Additionally, insufficient resistance to atmospheric and aqueous corrosion sometimes limits Mg-Al alloys applications in the fields of automobiles, aerospace, electronics, etc.[5–8] During the past two decades, there have been extensive efforts to increase the corrosion resistance of Mg-Al alloys. Much of the effort has concentrated on the use of various coating systems such as chemical conversion coatings, anodizing, gas-phase deposition processes electro- or electro-less plating, and organic coating.[9–15] Lowering the impurity levels, alloying, rare earth additions, and heat-treatment have also been explored to increase the corrosion resistance of these alloys.[16–20]

Alternative casting processes are being developed to resolve the mentioned problems and meet the requirements of future applications of Mg-Al alloys. Semi-solid metal (SSM) processing is a promising manufacturing route capable of producing castings with a high level of complexity.[21,22] The main advantage of SSM processing, compared to the conventional casting processes, is the possibility to have a laminar flow of metal during mold filling.[23] This is a consequence of the higher viscosity of the semi-solid material, and it reduces air entrapment compared to die-casting. This results in components with enhanced microstructural properties and improved mechanical properties.[24,25]

This paper deals with the microstructure and corrosion resistance of alloy AZ91D produced by the rheocasting (RC) technique, which is classified as a SSM process. RC is a casting process that offers cast components with very low pore content and a high strength when a strict temperature control is achieved.[26] One encouraging method for preparing the slurries for the RC technique is the newly developed RheoMetal process, which is also known as the Rapid Slurry Formation (RSF) process.[27] The RheoMetal process converts a molten metal into slurry using internal enthalpy exchange between the liquid metal at relatively low superheat and piece of solid metal attached to a stirrer.

Normally, the solid metal, called Enthalpy Material (EEM), Exchange is cast onto a steel rod. The rod is immersed into the melt during stirring after cooling down to moderate temperatures. Thereby, the melt is quickly cooled down during the melting of the EEM, and at the end, homogeneous slurry is prepared. An advantage of the RheoMetal process is that no external heat exchange is required, and accordingly the need for temperature control during slurry formation is eliminated.[26,27] The solid fraction is easily controlled in a robust way by the initial temperatures of the melt and the EEM as well as the EEM to melt ratio. The requirement that the slurry be pourable into the shot sleeve of a die casting machine requires at the solid fraction be controlled in the range 30–35%.

Due to the practical uses of alloy AZ91D in atmospheric conditions, a better understanding of the atmospheric corrosion properties, rather than immersion testing of Mg alloys, produced by different casting techniques is of importance.[28–35] Recently, it was reported that Mg alloy AM50 produced by the RC method, exhibited great potential in overcoming some of the inherent problems of conventionally cast Mg-Al alloys.[36] Thus, the ability to resist atmospheric corrosion during both constant and cyclic atmospheric exposures was better for RC AM50 compared to the same alloy in the HPDC state, especially at below-ambient temperatures. Methieu et al.[37] compared the corrosion behavior of alloy AZ91D in HPDC and SSM states in a solution with a pH of 8.2 and 10.6. They reported that the alloy produced by SSM exhibits a better corrosion resistance than HPDC material and attributed this behavior to the difference in the composition of α-Mg grains in the two alloys. However, there is limited knowledge on the microstructure and atmospheric corrosion behavior of the alloy RC AZ91D. Very recently, Mingo et al.[38] studied the corrosion resistance of alloy AZ91 produced by RC process using electromagnetic stirring in 3.5 wt% NaCl at pH 6.5. They compared the corrosion results of the RC AZ91D with those of the alloy produced by gravity casting (GC) and reported a better corrosion resistance of RC AZ91D.

This study is a continuation of the previous works on the influence of RC process on the microstructure[39] and corrosion resistance of Mg-Al alloys.[36,40] In this investigation, the microstructures of alloy AZ91D produced by RC and HPDC techniques are systematically characterized by statistical approaches using different image analysis software. The corrosion behavior of RC AZ91D and HPDC AZ91D are compared and the differences in corrosion rates are attributed to

*Electrochemical Society Student Member.
**Electrochemical Society Active Member.
zE-mail: mohsen.esmaily@chalmers.se

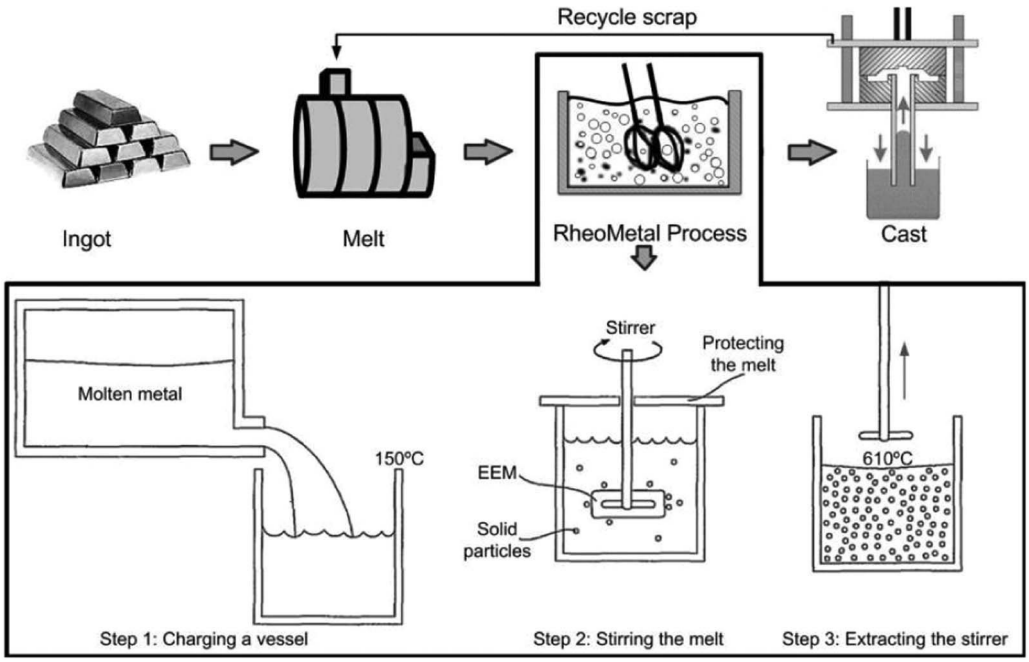

Figure 1. Schematic illustration of the RheoMetal process used for preparing the slurry required for the RC technique. This casting method was used in this study to produce the RC AZ91D material.

the differences in their solidification microstructures. Studying the microstructure and corrosion behavior of the alloys simultaneously provided unique insights into the dominating corrosion mechanisms in the two alloys.

Experimental

RC casting of Mg alloy AZ91D.— The RC casting machine used to produce the RC materials was made by Suzhou Sanji Foundry Co Ltd. The machine comes with a locking force of 50 tons. The designed die had a projected area of 250 cm^2 and the cast components had wall thicknesses of 7, 12 and 20 mm. The melt superheat was 42 ± 5°C and the EEM addition corresponded to about 4% of the shot weight. The EEM's, having a diameter of 38 mm, were produced by pouring liquid AZ91 in a cylindrical metal die into which stainless steel rods with a diameter of 12 mm were placed. The EEM, having a temperature of 140°C, was thereafter stirred at 1000 rpm in the liquid AZ91 for 12 seconds. The final slurry temperature was 593°C. The casting die temperature was maintained at 100–200°C. The gate velocity during cavity filling increased from about 6 m/s initially to 12 m/s at the end of the shot, and the total cycle time was around 60 sec for each casting. The RC process is schematically drawn in Fig. 1. A more detailed description of the casting machine and the process parameters can be found in previous papers.[27,39]

Sample preparation.— The chemical compositions of the RC and HPDC AZ91D are listed in Table I. Care was taken to produce samples from the HPDC and RC alloys from the same bar thickness (12 mm) and the same distance from the casting surfaces to compare the microstructure of the alloys tested. As-received materials were cut to produce 14×14×3 mm^3 corrosion samples with a surface area of 5.6 cm^2. For both microstructural characterization and corrosion experiments, the samples were first ground by SiC grit papers from P1000 to P4000 mesh. Polishing was performed using cloth discs and diamond paste in the range of 3–1 μm, following by a fine polishing step via OPS colloidal silica.

Table I. Composition (wt%) of the alloys investigated.

Material	Mg	Al	Zn	Mn	Si	Fe	Cu	Ni
RC AZ91D	Bal.	8.9	0.74	0.21	0.008	0.0022	0.0007	0.0004
HPDC AZ91D	Bal.	9.0	0.77	0.22	0.005	0.0015	0.0003	0.0002

Corrosion experiments.— The exposures were conducted at ambient (22.00 ± 0.3°C) and below ambient temperature (4.00 ± 0.3°C). The experimental set-up for the corrosion exposures in the presence of CO_2 are described elsewhere.[34] Relative humidity (RH) was regulated to be 95 ± 0.3% for the exposures performed at the two temperatures by mixing measured amounts of dry air and 100% RH air. CO_2 was added from a cylinder to give a constant concentration of 400 ± 20 ppm. The levels of particulate chloride (Cl^-) deposition reported in the literature cover a very wide range; 15 μg/cm^2y is reported in rural areas far from coast,[41] 60 μg/cm^2y for metropolitan New York,[41] and deposition rates of over 5500 μg/cm^2y have been found in extreme marine environments.[42] We contaminated the samples with 70 and 130 μg/cm^2 NaCl equal to 550 and 1020 μg/cm^2y of chloride ions, respectively, using a solution of distilled water, ethanol and NaCl. These values correspond to urban areas and to marine environments but not in the immediate vicinity of the coastline. It was noticed that the formation of NaCl solution droplets on the sample surface during salt deposition resulted in an uneven salt distribution with salt accumulating over the specimen's surface. In order to achieve an even distribution of salt, the spraying procedure was optimized with respect e.g. to the distance between the spray gun and by dividing the spraying into several steps with intermittent drying. Triplicate samples were used for each condition to assess the reproducibility of the data.

Gravimetric measurements.— At the conclusion of exposures, the samples were stored for 24 hours over a desiccant so that the loosely bound water was removed. They were weighed and the corresponding mass gains are termed dry mass gains. The metal loss values were determined using leaching and pickling processes. Thus, the samples were first immersed in Mili-Q water (ultrapure water) for 30 + 60 s at 25°C. Subsequently, the corroded samples were pickled several times in a chromate solution of 20% chromium trioxide (CrO_3) for 15 s followed by several periods of 30 s. The mass loss values were

obtained by the following equation:

$$M_{loss} = (M_O) - (M_P) \quad [1]$$

where M_{loss} is metal loss, M_O is mass before exposure and salt, M_P is mass after final stage of pickling (Cr-treatment). It should be mentioned that the gravimetric values were averaged from the data (3–8 samples for each test condition) with error bars based on one standard deviation.

Analytical techniques.— An FEI Quanta 200 environmental scanning electron microscopy (ESEM) equipped with Oxford Link energy dispersive X-ray (EDX) microanalysis hardware was used for metallographic observations and morphological inspections of the samples. Different magnifications and detectors (secondary electrons (SE) and backscattered electrons (BSE)) were used for imaging. Crystalline corrosion products formed under various exposure conditions and the microstructure of RC and HPDC AZ91D were analyzed by X-ray diffraction (XRD) using a Bruker AXS D8 powder diffractometer. The system was equipped with grazing incidence beam attachment and a Göbel mirror. CrKα radiation (λ = 2.29 Å) was used and the angle of incidence was 5°.

The X-ray Photoelectron Spectroscopy (XPS) analyses were conducted by means of a PHI 5500 instrument using an AlKα X-ray source (93.9 eV). Selected region spectra were recorded covering the C 1s, O 1s, Mg 2p and Al 2p photoelectron peaks. Curve fitting using the PHI Multipak software by assuming Shirley background was done to obtain chemical state information.[43] The acquisition conditions were 23.5eV pass energy, 45° take off angle and 0.1 eV/step. The depth profiling was carried out by means of successive 4 kV argon ion etchings and XPS analyses. The etch rate was calibrated by using Ta_2O_5 with known thickness under the same test condition. The concentration was calculated from the peak areas assuming Shirley background using $Cx = (I_x/S_x)/(\Sigma Ii/Si)$, where I_x is the intensity of element X, S_x the atomic sensitivity factor of each photoelectron provided by the instrument manufacturer.[43]

Several programs, Adobe Photoshope CS4, Image Pro-Plus and ImageJR, were used to carry out statistical analyses on the microstructure of the alloy AZ91D produced by the HPDC and RC methods. Microstructural quantifications were performed to quantitatively characterize the differences in the microstructure of the alloys. All the microstructural features were quantified using etched and non-etched samples. The etching was done using a solution of Nital (5 ml HNO_3 + 95 ml ethanol) as the etchant to reveal the microstructure. The grain size measurments were carried out based on the Feret diameter or Feret's diameter, which is a measure of an object or particles size along a specified direction. In the case of microstructural studies, the Feret diameter is defined as the distance between two parallel tangential lines rather than planes.[37]

A Leica EM TIC 3X broad ion beam milling (BIB) system was used to produce cross sections in order to study the morphology of corrosion products. The system was equipped with an OM to find the region of interest for milling. The BIB method is able to produce planar and accurate cross sections with a minimal amount of artifacts. BIB can produce wide cross sections, which provides suitable statistical information. Considering the large surface area (up to around 1.5 mm in width and several hundred microns deep) of the cross sections produced by BIB, the method was very well-suited to studying corrosion pits on heavily corroded samples. Sample preparation can be problematic when studying a corrosion layer on the metal surface. The sample was first cut to obtain a smaller piece that can be fitted inside the BIB sample holder using a low speed saw. Lubricant was not used to avoid artifacts and further damages to the corroded surface. A shield plate, which is termed "blade" in the Fig. 2, was used to achieve a smooth cross section. A silicon plate was glued using TEM glue (M-bond 610) to the corroded sample for protection prior to cutting. Finally, the sample was mounted to the blade with silver glue. The ion gun was operated at 6 KV and the sputtering time was about 8 h.

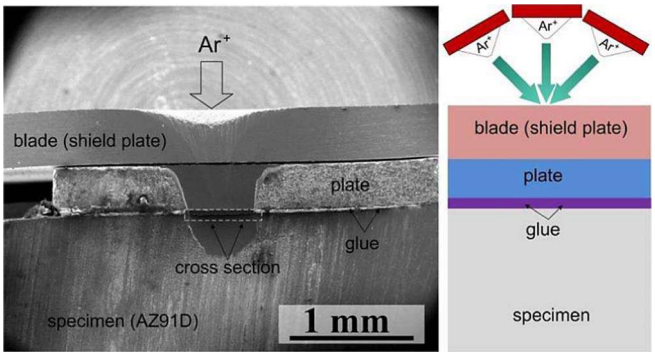

Figure 2. Showing a large BIBed cross section (of about 500 μm) of a corroded sample (in the left image) as well as a schematic of the different layers applied on samples for obtaining a smooth cross section through the corrosion product and metal substrate (in the right image).

A LEO Ultra 55 field emission gun SEM equipped with an HKL Channel 5 electron backscatter diffraction (EBSD) system was used to perform orientation mapping on the microstructure of the RC and HPDC alloys. EBSD maps were obtained from longitudinal cross sections of the RC and HPDC materials. Samples were first mechanically polished, according to the above procedure, and then cold-stage argon-ion-beam milled using a Gatan PIPS instrument. A gun tilt of 12° was used together with settings of 4 kV and 0.8 mA and a milling time of 3 hours. The SEM was operated at 20 kV during EBSD analysis with the sample tilted to 70° on the cross section of the castings (taken from the bar with a thickness of 20 mm). The mappings were performed using a step size of 0.6 μm.

Results

Microstructural analysis.— The microstructure of Mg-Al alloys, especially AM50 and AZ91D, has been described by several authors.[44,45] The main microstructural constituents are α-Mg grains (hexagonal; P63/mmc, a = 0.32 nm, c = 0.521 nm) surrounded by inter-dendritic regions (also called eutectic α) and β phase particles ($Mg_{17}Al_{12}$, cubic; 14 $\bar{3}$ m, a = 1.056 nm). Owing to the presence of Mn, Mg-Al alloys in the AM and AZ series also contain a small amount of η phase particles ($Al_8Mn_{5-x}Fe_x$).[46] In addition, transient phases such as Mg_5Al have been reported in the cast microstructure of alloy AZ91D.[47] This is a precursor of β-$Mg_{17}Al_{12}$ and has considerably lower volume fraction than the dominant intermetallic phase particles. Figure 3 shows SEM micrographs and EBSD maps of the microstructure of AZ91D in RC and HPDC states. In both cases, the β phase component appeared in the inter-dendritic regions, showing network-type morphology. This microstructural configuration is typical for as-cast AZ91D. A comparison of the microstructures produced by RC and HPDC techniques showed that the β phase tends to form relatively fine, dispersed particles in the HPDC material while the β phase particles in the RC alloy are coarser and more continuous, see Figs. 3a and 3b. The inverse pole figure (IPF) images that were obtained from the EBSD analysis, presented in Figs. 3c and 3d, clearly shows that the α-Mg grains were larger in RC AZ91D than in the HPDC material, both alloys exhibiting dendritic α-Mg grain morphology. It may be noted that the α-Mg grain morphology in the studied RC AZ91D differs from the globular α-Mg morphology (with high aspect ratio) observed in the microstructure of a RC AZ91 material where the slurry was made by electromagnetic stirring.[38]

EBSD mapping provided an opportunity to evaluate the low angle grain boundaries (LAGBs), boundaries with a misorientation < 15°, in the alloy microstructure. When an LAGB exists between two grains, the grain boundary can be described by a relatively simple configuration of process-induced dislocations for instance edge dislocation walls or cells.[39] Thus, a high fraction of LAGBs specifies

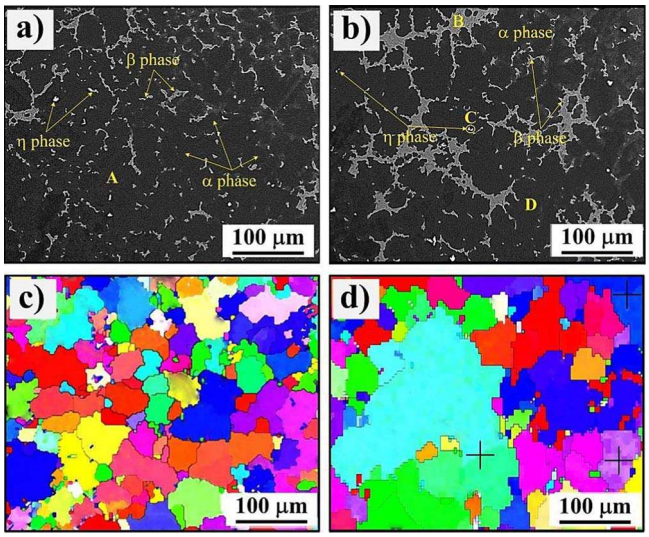

Figure 3. SE-SEM image and EBSD grain mapping showing typical microstructures of alloy AZ91D produced by HPDC and RC techniques; (a and c) HPDC AZ91D and (b and d) RC AZ91D. EDX point analysis of A, B, C and D are presented in Table II. Note: the EBSD maps and the SEM images show different regions. The deformed grains in the microstructure of the RC AZ91D alloy in Fig. 3d are marked by crosses.

some degree of deformation in a metal's microstructure. The fraction of LAGBs in the microstructure of the RC material was about 9%, compared to about 4% in the microstructure of the HPDC material. This indicates that some α-Mg grains in the as-cast microstructure of the RC material were slightly deformed. Accordingly, Fig. 3d shows several deformed α-Mg grains (indicated by crosses). It is suggested that the slightly deformed grains in the RC AZ91D formed during slurry preparation and during the passage into the die cavity. Similar observations on the effect of casting technology on microstructure have been reported for alloy AM50 produced by RC and HPDC techniques.[39]

The EDX point analysis in Figs. 3a and 3b are summarized in Table II. The α-Mg grains had significantly different Al concentrations in the HPDC and RC materials. Thus, the Al content in the middle of α-Mg grains in the HPDC alloy (point A) and in the RC alloy (point D) were 2.4 and 3.8 wt%, respectively. To investigate the difference in Al content of α-Mg grains in the two materials, EDX analyses were carried out on 20 α-Mg grains (size range 10 to 20 μm) in the two alloys. The average Al content in the α-Mg grains was 2.6 ± 0.1 wt% in the HPDC material while the corresponding value for the RC alloy was 3.95 ± 0.22 wt%. Both values were higher than the room temperature solubility of Al (∼ 1.5 wt%) in Mg, indicating that the α-Mg grains were slightly supersaturated. The chemical composition of Point B in Fig. 3b suggests that the gray phase is β-$Mg_{17}Al_{12}$ containing some Zn in solid solution. In Mg-Al-Zn alloys, Zn is enriched in the β phase, substituting for a part of Al and forming $Mg_{17}(Al,Zn)_{12}$ or $Mg_{17}Al_{11.5}Zn_{0.5}$ at temperatures below 437°C.[48,49] The Mg/Al ratio 1.62 (60.5/37.4) of the β phase was somewhat higher than the stoichiometric ratio, 1.49 (17/11.5). The high Mg analysis is attributed to

Table II. Typical composition of the main phases (wt%) of the points designated in Fig. 3.

Point	Mg	Al	Mn	Zn
A (α-Mg HPDC)	97.15 ± 1.2	2.4 ± 0.04	-	0.45 ± 0.01
B (β $Mg_{17}Al_{12}$)	60.5 ± 0.5	37.4 ± 0.42	-	2.1 ± 0.02
C (η AlMn)	3.9 ± 0.1	47.1 ± 0.23	49 ± 0.55	-
D (α-Mg RC)	95.5 ± 0.7	3.8 ± 0.15	-	0.7 ± 0.01

contributions from the α-Mg solid solution matrix.[50,51] The fine white particles (point C in Fig. 3a) were a compound of Al and manganese (Mn) (Table II), i.e. Al_8Mn_5.

To further elucidate the microstructural differences between HPDC and RC materials, quantification studies were performed (Fig. 4). Figure 4a shows the α-Mg grain size distribution profiles of the microstructure of the RC and HPDC materials. In the RC material, the α-Mg grains covered a wide size range from a few microns to more than 120 μm. In contrast, few coarse grains (>100 μm) were observed in the HPDC alloy. Hence, the RC material exhibited larger α-Mg grains than the HPDC material, in accordance with Figs. 3c and 3d. Thus, the average grain size (determined based on Feret diameter) was measured to be about 32.4 ± 5 and 21.3 ± 3 μm in the RC and HPDC materials, respectively. Also, the coarse grains occupied a significantly larger area fraction in the RC material. The coarse α-Mg grains in RC AZ91D were frequently observed to be surrounded by much finer grains, in the size range 2–10 μm. Thus, the HPDC alloy exhibited a more uniform microstructure than the RC material.

Figure 4b presents the size of the β phase intermetallic particles in the investigated regions of RC and HPDC AZ91D. Perhaps the most striking difference between the microstructure of the two materials is related to the β phase particles. In accordance with the SEM images (Figs. 3a and 3b) that show a more continuous and network-like morphology for the β phase in RC AZ91 compared to the HPDC material, the statistical analysis showed that larger β phase particles form in the RC material. In the case of HPDC AZ91D, more than 78% of the β particles were fine particles in the range <150 μm^2. In contrast, RC AZ91D exhibited a large fraction of medium size and coarse β particles, in the range >150 μm^2. The β phase fraction was higher in the RC material than in the HPDC material, being around 9.5 and 6.8% for the RC and HPDC materials, respectively. The higher fraction of β phase in the RC material compared to the HPDC material can be qualitatively seen in Figs. 3a and 3b. This is in accordance with a recent study[39] on the effect of RC processing on the microstructure of alloy AM50, where the same trend in the fraction of β phase intermetallic particles was reported for the RC and HPDC materials. It may be noted that there was a significant difference in the number density of β phase particles in the two alloys in the investigated area (1.97 mm^2). The calculated total number of β phase intermetallic particles detected was 1152 and 504 1 particles/mm^2 for HPDC and RC AZ91D, respectively.

While the fraction of β phase was higher in the RC than in HPDC material, it is cautioned that the measured fractions of β phase were obtained from one cross section of the castings and may not be representative of the entire RC and HPDC materials. Figure 4c shows quantitative data on the η phase particles in both materials. The size distribution of these particles was nearly the same in the two materials, the η phase particles exhibiting an area fraction of 0.48 ± 0.05% for both alloys. This implies that that the casting technique did not influence the size of η phase particles significantly. Figure 4d presents the size distribution of pores in RC and HPDC processed alloy AZ91D. To facilitate comparison, the results are divided into three sections; fine, medium and coarse. While both materials revealed defect bands more or less parallel to the cast skin having a high fraction of pores, the fraction of porosity in the HPDC material was slightly more than 2 times greater than in the RC AZ91D alloy. In the case of RC AZ91D, pores were frequently associated with the melt solidified in the interdendritic regions, the morphology being similar to that reported in.[39] Macro-porosities corresponding to large gas pores (coarse pores in Fig. 4d) in the range > 180 μm^2 were more frequent in the HPDC material.

As expected, the XRD patterns of as cast alloy AZ91D in Fig. 5 showed strong diffraction from α-Mg and weaker β-phase peaks in both the RC and HPDC states. The XRD analysis showed no evidence of the AlMn (η) phase due to its low area fraction. Figure 5 shows that the β phase peaks had a higher relative intensity for the RC material than for HPDC AZ91D, confirming that the area (and volume) fraction of β phase is higher in the RC material.

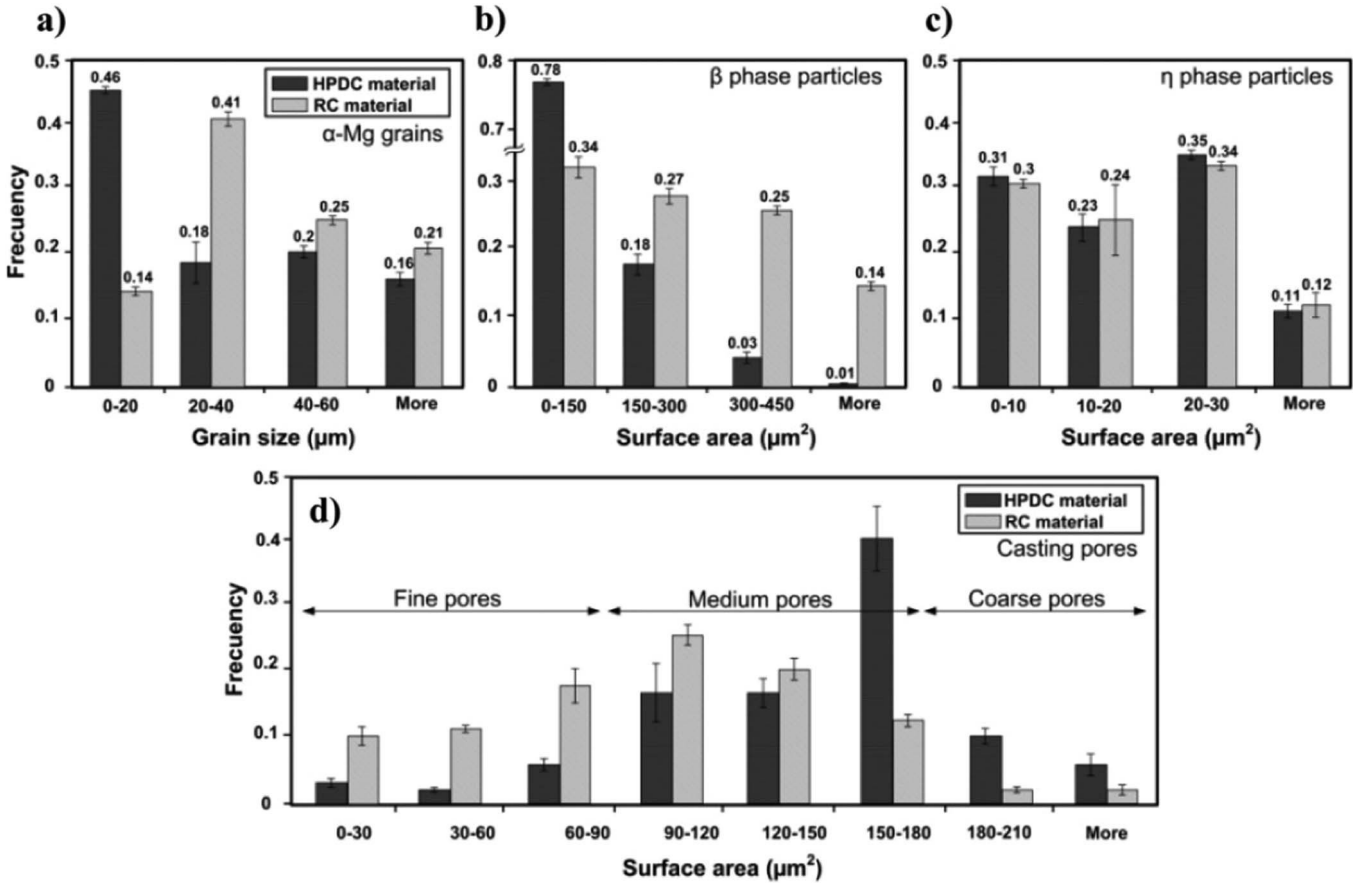

Figure 4. Size distribution of microstructural features including α-Mg grains, intermetallic particles and porosity in RC and HPDC AZ91D, (a) size distribution of α-Mg grains, (b) size distribution of β phase, (c) size distribution of η phase and (d) size distribution of porosities in the both materials. The total number of intermetallics for HPDC and RC alloys was 1152 and 504, respectively, in the studied regions. (Note: frequency can also be defined as the percentage (%) of the total value observed).

Corrosion behavior of alloy AZ91D.—Comparing RC and HPDC AZ91.—The dry mass gains as a function of exposure time (time intervals from 10–1176 h) for both RC and HPDC materials are presented in Fig. 6. Mass gain is a convenient way to measure average corrosion attack if the corrosion product composition is known and if the corrosion products remain on the surface. Also, mass gain measurements are useful for comparing the corrosion rates of materials if the corrosion products have similar composition, which is the case here. A relatively large amount of salt (130 $\mu g/cm^2$) was deposited on the samples before exposure in order to accelerate corrosion. The results showed that, at all exposure times, the mass gains of the RC alloy were smaller than for HPDC AZ91D, Thus, RC AZ91D exhibited significantly better corrosion resistance than HPDC AZ91D.

The mass gain curves reveal that the two materials exhibit somewhat different corrosion kinetics. In the early stages of corrosion both materials showed approximately linear mass gain curves, corresponding to a constant rate of corrosion, (see Figs. 6a; <30 h and 6b; <144 h). An inspection of Fig. 6c shows that both mass gain curves become convex after longer exposure, which corresponds to a deceleration of the corrosion process. The deviation from linear behavior becomes apparent after 504 h (3 weeks) for the RC alloy while it is seen only after about 840 h (5 weeks) for the HPDC material. The tendency of the slowing down of corrosion to set in earlier for the RC material than for the HPDC alloy contributes to the relative superiority of the corrosion behavior of the RC material. Thus, after 1176 h (7 weeks) exposure, the mass gain (= average metal loss) of the RC alloy was only about 40% of the alloy in the HPDC state.

The corrosion behavior of alloy AZ91D in HPDC and RC states was examined at two temperatures (22 and 4°C). The rate of atmospheric corrosion depended strongly on exposure temperature. Thus, increasing the temperature from 4 to 22°C resulted in an increase in the corrosion rate of RC and HPDC AZ91 by a factor of 3.5 and 2.5, respectively. Accordingly, Fig. 7 shows that the samples exposed at 4°C were only less corroded, showing fewer and smaller corrosion products on the surface. The strong dependence of corrosion on temperature is also in line with the observation that while there was little evidence for NaCl remaining on the surface after 672 h at 22°C, large amounts of NaCl crystallites remained after exposure at 4°C. The amount of recrystallized salt after 672 h exposure at 4°C is especially seen for the case of RC AZ91D, indicating the better corrosion resistance of RC AZ91D than HPDC AZ91D at below ambient temperature. The influence of temperature on the corrosion behavior of Mg-Al alloys has been studied elsewhere.[34]

Figure 8 shows the BIB-prepared cross sections of RC and HPDC AZ91 after exposure at 22°C in the presence of 130 $\mu g/cm^2$ NaCl. After plasma cleaning, the cross sections were analyzed by EDX. The dark regions in Fig. 8 correspond to corrosion products with the following composition; Mg (17 ± 0.2 at.%), O (64 ± 1.2 at.%), C (18.8 ± 0.4 at.%) and a Al (0.2 ± 0.05 at.%). The resulting C/O ratio of ~ 0.29 and Mg/O ratio of ~ 0.26 are similar to the corresponding ratios of Mg hydroxy carbonates identified by XRD (see below). The SEM image in Fig. 8a shows a cross section of a corroded HPDC AZ91D sample after 840 h. The thickness of the corrosion product layer is about 100 μm. In the regions close to the sample surface, all the α-Mg grains and inter-dendritic regions are completely corroded and only β particles remain. In this manner a "barrier layer" consisting

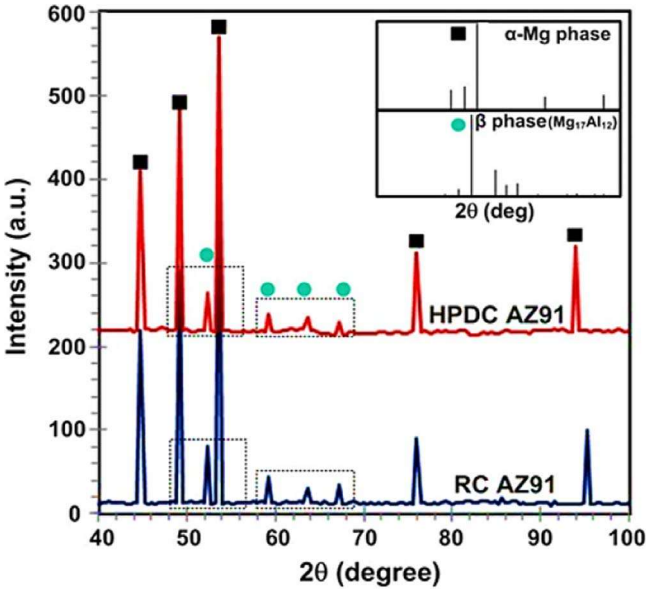

Figure 5. XRD patterns for as-cast RC and HPDC AZ91. The X-ray diffraction peak positions for α-Mg and β phase are also shown.

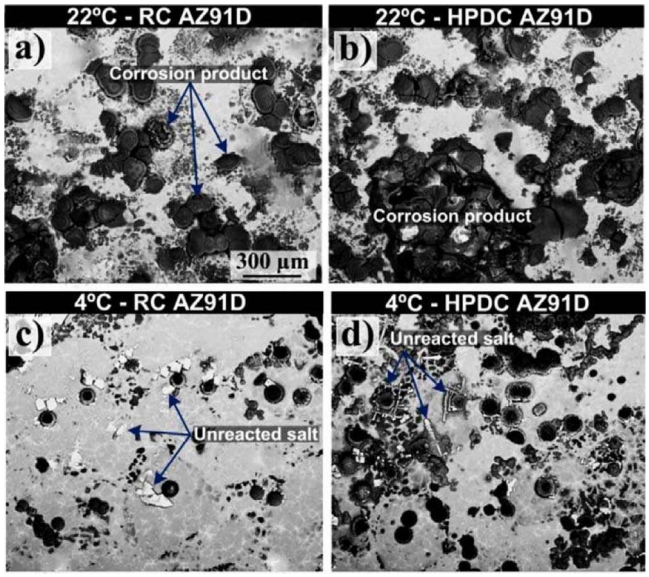

Figure 7. SEM micrographs showing representative images of HPDC and RC AZ91D samples after 672 h exposure in air at 95% RH and 400 ppm CO_2. Temperature was 22, 4°C. 70 μg/cm^2 NaCl was added before exposure.

of slowly corroding β phase tended to form on the alloy surface. An inspection of the cross sections in Fig. 8 shows that, due to the greater connectivity of the β phase, the "barrier effect" is more pronounced for the RC alloy than for the HPDC material, compare Figs. 8b and 8c. The barrier effect is also treated below, in the discussion.

Corrosion product composition.—The corrosion products formed were investigated by XRD (not shown) on HPDC and RC AZ91D. The same crystalline corrosion products were identified on both alloys as the chemical composition of the alloys were identical. The XRD diffractograms were the same as the ones reported in a previous paper.[34] The corrosion products identified by XRD at 4 and 22°C were identical. In addition to the main corrosion product, which was $Mg_5(CO_3)_4(OH)_2\times4H_2O$ (hydromagnesite), there was also evidence for $Mg_5(CO_3)_4(OH)_2\times5H_2O$ (dypingite) and $Mg_5(CO_3)_4(OH)_2\times8H_2O$ (giorgiosite).

The chemistry of the surface films formed on alloy AZ91 in RC and HPDC states was examined by means of XPS depth profiling on the middle of α-Mg grains (with ~ 20 μm diameter) in the two

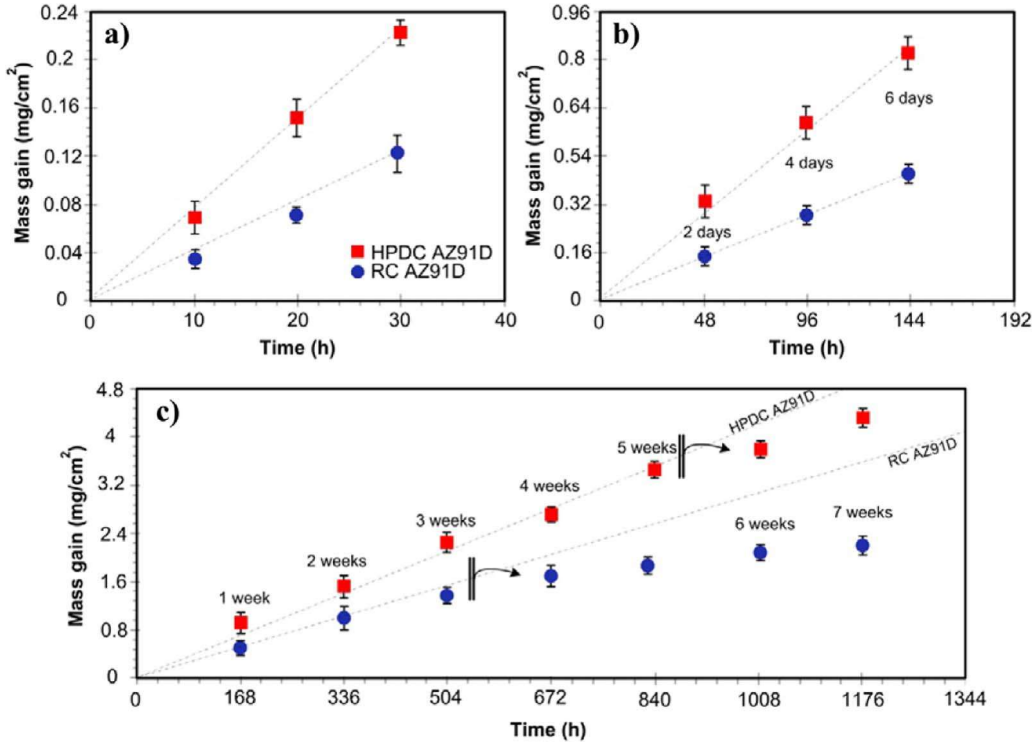

Figure 6. The effect of casting method on the mass gain of alloy AZ91D in 95% RH air containing 400 ppm CO_2 at 22°C. 130 μg/cm^2; of NaCl was added before exposure; (a) up to 30 h, (b) up to 144 h, (c) up to 1176 h.

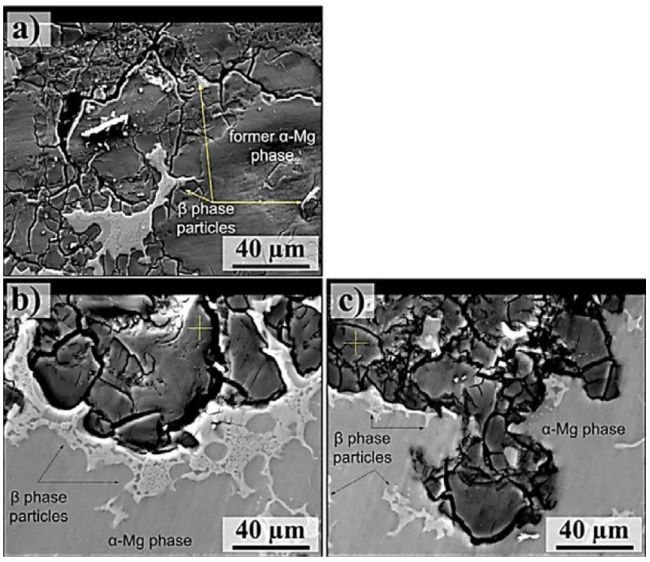

Figure 8. SEM-BSE images of BIB-cross sections of alloy AZ91D after exposure in 95% RH air with 400 ppm CO_2 at 22°C. 130 µg/cm^2 NaCl was added before exposure (a) HPDC alloy AZ91D after 840 h, (b) RC alloy AZ91D after 504 h exposure and (c) HPDC alloy after 504 h.

alloys after 672 h corrosion exposure, see Fig. 9. The samples were exposed to 95% RH air with 400 ppm CO_2 at 22°C in the absence of NaCl. As expected, the mild environment caused very slow corrosion (the mass gains registered after 672 h (4 weeks) corresponding to an average corrosion rate of < 0.4 µm/year). For ease of comparison, the profiles are divided into three zones. The first zone (I) corresponds to the surface, showing a high atomic percentage of C. The second zone

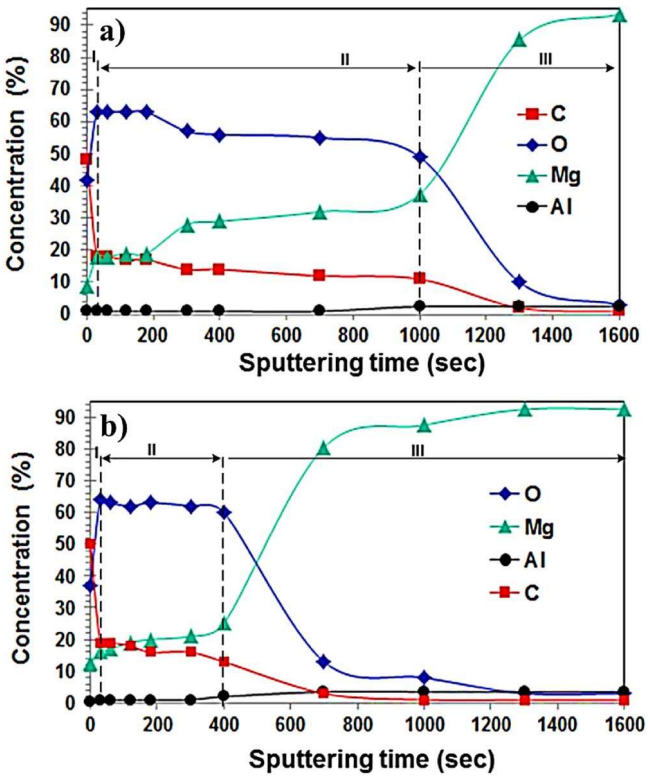

Figure 9. Elemental distribution by XPS depth profiling of α-Mg grains in alloy AZ91D after 672 h exposure in 95% RH air with 400 ppm CO_2 at 22°C. The exposures were performed in the absence of NaCl. (a) HPDC AZ91D and (b) RC AZ91D.

(II) is dominated by Mg, O and C and corresponds to the corrosion product layer. In zone III the O signal is weak and the signals from Mg and Al strong, corresponding to the alloy substrate. A comparison of the two profiles shows that the corrosion product film (zone II) is significantly thicker on the HPDC material (Fig. 9a) than on RC AZ91D (Fig. 9b).

As expected, the two corrosion product layers had similar composition. Thus, zone II in Fig. 9b and the outer part of zone II in Fig. 9a both contained 60–65% O, about 15% C and 15–20% Mg. The XPS analysis is compatible with the presence of magnesium hydroxy carbonate in the surface film, as identified by XRD and high-resolution XPS in Figs. 9a and 9b. For example, the composition of hydromagnesite corresponds to 67% O, 15%Mg and 18% Mg (not counting hydrogen). It may be noted that the corrosion product film contained small amounts of Al, on the order of 1%. In Fig. 9a, the bottom part of zone II is somewhat poorer in O and C, suggesting a different corrosion product composition.

Given the rate of sputtering, the corrosion surface film was calculated to be ~ 25 nm for RC AZ91D and ~ 46 nm for HPDC AZ91D. These values can be compared to the average film thickness obtained from the mass gains. The dry mass gain of the materials in Fig. 9 was ~ 4.9 and 8.4 µg/cm^2 for the RC and HPDC material, respectively. Assuming hydromagnesite to be the dominant corrosion product, the average film thickness was calculated to be ~ 35 and 61 nm for the RC and HPDC materials, respectively. Considering that some local corrosion attack may had occured, these values are in good agreement with the film thickness obtained by depth profiling.

Discussion

The influence of casting technology on alloy microstructure.— The results show that the corrosion properties of alloy AZ91D can be significantly improved by changing the solidification microstructure through the casting process. To understand the causes behind this effect it is necessary to first discuss the differences in the microstructural configuration of alloy AZ91D produced by conventional HPDC and RC AZ91D. The solidification process in both the HPDC and RC techniques is far from equilibrium due to the rapid melt cooling and is described by the Scheil equation.[52,53] Thus, the β-phase forms during solidification of HPDC Mg-Al alloys with Al contents >2%, even though the solid solubility of Al in α-Mg is about 13% at the eutectic temperature. Also, during subsequent cooling in the solid state, the solubility of Al in the α-Mg phase decreases to about 1.5% at ambient temperature. Hence, there is a driving force for precipitation of β-phase in the solid state. The latter process is observed in sand mold casting, where cooling is very slow.[54] In contrast, solid state precipitation of β does not seem to take place to any significant extent in RC or HPDC cast AZ91D, apparently due to the slow diffusion of Al and the fast cooling in the metallic molds.

According to the Mg-Al equilibrium phase diagram, solidification of alloy AZ91D with around 9% Al starts by the formation of primary α-Mg with an Al-content of about 2%. The EDX results showed that the average Al content of primary α-Mg grains is 2.4 and 3.8% for the case of the HPDC and RC materials, respectively (see Table II). It has been reported that the Al content of α-Mg cores in Mg-Al alloys depends on alloy composition and on the casting technique.[55–57] In the RC technique, an excess of solid fraction is generated during slurry preparation. These α-Mg particles have a solidus temperature corresponding to the liquidus temperature of the alloy, suggesting that they melt only by diffusion of Al into them. These particles tend to homogenize and it is likely that their composition (Al-content) corresponds to the phase diagram composition at the slurry temperature, or somewhat lower in Al. The slurry is kept at this temperature for 10–20 seconds before it is injected and the remaining liquid then solidifies in a normal way, following Scheil segregation. The slurry temperature and the composition of the slurry particles are determined by the alloy composition and the amount of EEM added.

As described above, the rate and mode of solidification have considerable impact on the microstructure of Mg-Al castings. Thus, in

comparison to conventional die-casting that results in a very fine microstructure because of the rapid solidification, semisolid casting gives rise to a coarser microstructure due to its special solidification mode. Accordingly, RC alloy AZ91 exhibits a coarser microstructure than the HPDC material, see Figs. 3 and 4. The microstructures of both RC and HPDC alloys contain externally solidified dendritic grains (ESGs) in the size range $> \mu m$ 40, and finer grains designated internally solidified grains (ISGs). The relatively coarse microstructure in the RC material compared to the HPDC alloy is related to the formation of these two types of grains. In the HPDC material, the ESGs correspond to grains that nucleate and grow in the shot sleeve prior to the melt entering the die, whereas the ISGs are fine, rounded grains formed in the die cavity. In the examined RC alloy, the ESGs form during slurry preparation. The formation of ESGs in the RheoMetal process may involve both adiabatic freeze-on of melt onto the EEM (as it is inserted into the melt to generate the slurry) and the subsequent partial melting of both the freeze-on layer and the EEM. In addition, RC AZ91D produced by the RheoMetal process contains ESGs that have nucleated and grown in the shot sleeve. It was noticed that, in the area close to the shot sleeve wall, the fraction of ESGs in the microstructure of the RC and HPDC materials reaches as high as 73 and 39%, respectively, confirming the coarser microstructure of the RC 91AZD compared to HPDC AZ91D.

Interestingly, even though the two materials had essentially the same composition with about 9% Al content, RC alloy AZ91D had a higher β phase fraction than the HPDC material. Also, the β phase tended to form larger and more connected particles in the RC material. The higher β phase fraction in the RC material was shown by statistical analyses (Fig. 4b) and by XRD (Fig. 5). The exact cause behind this discrepancy is not fully understood. However, in the case of alloy AM50, we previously showed that the fraction of inter-dendritic regions was higher in the HPDC material compared to the RC alloy.[39] Similar behavior is expected for alloy AZ91D produced by RC and HPDC techniques. Therefore, it is suggested that the solidification process in the HPDC technique tends to generate a high fraction of Al-rich inter-dendritic regions, rather than β phase particles. Conversely, the special solidification characteristics (micro-segregation, cooling rate, etc.) of the RC technique are favorable for the formation β phase particles. Indeed, the formation of larger more network-like β phase particles in RC AZ91D can be ascribed to the rather complex solidification characteristic in the RheoMetal process. Thus, grain growth occurs during the controlled cooling of the melt to form the semi-solid, through the addition of EEM. During the secondary solidification in the die cavity, all the eutectic is concentrated in the liquid regions between the ESGs.

A consequence of the non-dendritic morphology, which is a known microstructural characteristic of semi-solid casting, is that the solid-liquid interfacial area becomes smaller, meaning that the β phase growth will be less restricted than in the case of the HPDC material. This explains why the β phase forms large continuous particles in the RC alloy rather than fine disperse particles as in the HPDC material.

The microstructural characterization indicated that the fraction of pores in HPDC AZ91D was about twice that of the RC material. Casting pores in HPDC Mg alloys typically include both entrapped gas bubbles and cracks caused by hot tearing.[58] Working with the microstructure of RC AZ91D, Fan et al.,[59] reported similar observations. Controlling the formation of porosities is extremely important from the mechanical properties point of view as they deteriorate the tensile and compression strength of the material.[60] It is reported that trapped gas bubbles form during filling while shrinkage defects occur when feed metal is not accessible to compensate for shrinkage as the metal solidifies.[61,62] Here, the RC process induces strong shearing forces on the slurry, and thus, the feed rate of the casting increases. This results in relatively quick fill speeds at high pressure. Hence, in accordance with the present results, the risk for pore formation caused by trapped gas as well as by shrinkage is expected to be less in RC AZ91D. The low temperatures and high apparent viscosity of the semi-solid slurry also leads to less porosity in castings made by the RC technique.

Corrosion of alloy AZ91D produced by RC and HPDC techniques.— Before going into the details of the effect of microstructure on the corrosion of alloy AZ91D produced by the RC and HPDC techniques, it is appropriate to shortly mention the corrosion properties of the alloy in humid air, in the presence of NaCl. The NaCl added to the samples prior to exposure absorbs water vapor to form a solution that comprises about 8% NaCl by weight (at 95% RH).[63] During immersion in NaCl (aq), Mg alloys are reported to suffer electrochemical corrosion involving anodic dissolution of Mg (2) and cathodic reduction of water (3).The dominant corrosion product in NaCl (aq) solution is reported to be brucite (4);[64–68]

$$Mg\,(s) \rightarrow Mg^{2+}\,(aq) + 2e^- \quad [2]$$

$$2H_2O + 2e^- \rightarrow H_2\,(g) + 2OH^-\ (aq) \quad [3]$$

$$Mg^{2+}\,(aq) + 2OH^-\ (aq) \rightarrow Mg(OH)_2\,(s) \quad [4]$$

The electrochemical process causes an accumulation of Cl^- (aq) at the anodic sites. This is expected to promote corrosion because Cl^- has been reported to enhance the dissolution of Mg in neutral solution.[69,70] The corrosion attack is also known to be stabilized by the metal cation hydrolysis and Cl^- migration toward anodic sites.[71,72] In the cathodic areas, hydroxide is produced and Na^+ (aq) ions are accumulated, resulting in high pH values, stabilizing the $Mg(OH)_2$ passive film. The overall corrosion reaction 2–4 becomes 5;[67,68]

$$Mg\,(s) + 2H_2O\,(aq) \rightarrow Mg(OH)_2\,(s) + H_2\,(g) \quad [5]$$

While the atmospheric corrosion of Mg alloys in the presence of NaCl at RH = 95% is expected to proceed in a similar way, there are significant differences in comparison to corrosion during immersion because of the small amount of aqueous solution available and the absence of large scale convection. Micro-galvanic elements are established where the anodic dissolution mainly occurs in the middle of the primary α-dendrite grains and the cathodic process mainly occurs on the intermetallic phases.[2] When Mg and its alloys are exposed to the ambient atmosphere, the main corrosion products are reported to be Mg hydroxy carbonates rather than brucite, indicating that CO_2 plays a key role in the atmospheric corrosion of Mg.[73] When CO_2 dissolves in water, it forms carbonic acid (H_2CO_3 (aq)). In alkaline conditions carbonic acid forms carbonate according to 6 and 7. CO_2 also reacts with brucite forming Mg hydroxy carbonates, see e.g. reaction 8;

$$H_2CO_3\,(aq) + OH^-\ (aq) \rightarrow HCO_3^-\ (aq) + H_2O\,(aq) \quad [6]$$

$$HCO_3^-\ (aq) + OH^-\ (aq) \rightarrow CO_3^{2-}\ (aq) + H_2O\,(aq) \quad [7]$$

$$5Mg(OH)_2\,(s) + 4CO_2\,(aq) \rightarrow Mg_5(CO_3)_4(OH)_2 4H_2O\,(s) \quad [8]$$

Accordingly, three different Mg hydroxy-carbonates were identified after exposures of alloy AZ91D at 4 and 22°C (see the schematic illustration in Fig. 10). The formation of carbonates on the surface film in the same exposure condition has also been detected by Fourier Transform Infrared Spectroscopy (FTIR) in the case of alloy AM50.[34]

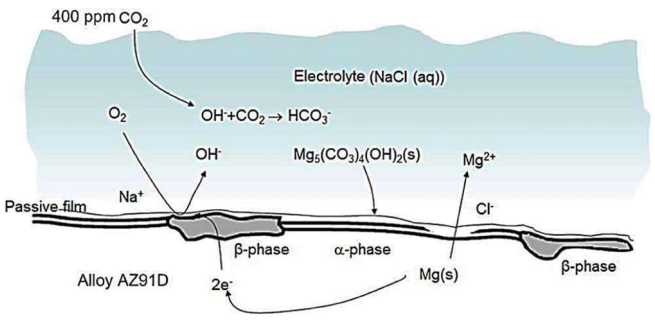

Figure 10. Schematic illustration of the corrosion of Mg-Al alloys in humid air in the presence of NaCl and ambient level of CO_2.

The nature of the surface film formed on Mg and Mg alloys in different corrosive environments has been widely studied.[54,74–78] In the present work, XPS depth profiling (Fig. 9) showed that the surface film formed on alloy AZ91D, in the absence of salt, in 95% RH air with 400 ppm CO_2 was mailnly composed of Mg hydroxy carbonates. The latter compounds also dominated in the corrosion products formed in humid air in the presence of NaCl, as confirmed in this study by XRD experiment.

In summary, the quantitative microstructural analyses shows that the RC material generally exhibits a coarser microstructure than the HPDC material, both the α-Mg and β phase particles being larger in the RC alloy. In contrast, the area fraction and size distribution of the η phase particles was apparently not influenced by casting technology. Below, we discuss the role of individual microstructural features, including the phase distribution and casting pores, on the corrosion of the alloy AZ91D.

The role of the α-Mg grains.—It has been reported that finer α-Mg grains are preferred in Mg-Al alloys from the corrosion point of view. Thus, Daloz et al.[79] reported that by modifying the microstructure of Mg-Al alloys using rapid solidification, the corrosion behavior was changed from pitting corrosion to general corrosion. In a similar way, Song et al.[80] argued that finer α-Mg gains and more continuous β-phase particles lead to better corrosion resistance. Song also reported that the fraction and connectivity of β-phase particles in the alloy microstructure was likely related to the size of the α-Mg grains. Also, in a recent investigation of the corrosion behavior in 1.6 wt% NaCl solution of alloy AM50 produced by sand, graphite and die casting, Asmussen et al.[81] report that the more fine-grained die cast alloy showed better corrosion resistance than the alloys produced by sand and graphite casting. In contrast, the present results show that while the α-Mg grains are larger in the RC material than in the HPDC alloy, the RC alloy shows significantly better corrosion resistance than HPDC material. This indicates that the size of the α-Mg grains is not a decisive factor for the corrosion of the alloy examined.

XPS depth profiling (Fig. 9) showed that the surface film formed on the α-Mg grains in humid air in the absence of NaCl, was thinner in the case of the RC material than for HPDC AZ91D. It is suggested that the thickness of the film, which mainly consisted of Mg hydroxy carbonate, was related to the Al content of the α-Mg grains. Thus it is suggested that the higher Al content in the α-Mg grains in the RC material results in the formation of a more protective surface film containing a higher amount of Al^{3+} compared to the the HPDC alloy. Also, it is suggested that the more protective α-Mg surface film can partly explain the initially relatively slow atmospheric corrosion of RC AZ91D in the presence of NaCl.

The role of β phase particles.—Lunder et al.[82] reported that the corrosion potential of β-phase in 5% NaCl (aq) saturated with $Mg(OH)_2$ is cathodic to pure Mg and to alloy AZ91 by about 490 and 420 mV, respectively. Thus, the cathodic reduction of water is expected to preferentially take place on the β phase. On the other hand, as pointed out by Song et al.,[80] β-phase particles can also act as a corrosion barrier in Mg-Al alloys. Our results show that; (a) the fraction of β phase particles was about twice as high in the RC material compared to the HPDC alloy, (b) the size of the β phase particles was related to the casting technology rather than to the size of the α-Mg grains, (c) the degree of connectivity of the β phase particles was higher in the RC alloy, and (d) the number density of β phase particles was higher in the HPDC material than in the RC alloy. As explained below, these observations imply that the β phase plays a dual role in the corrosion of the HPDC and RC materials, see also the schematic image in Fig. 11.

In the initial stages of corrosion, the faster corrosion of HPDC alloy in comparison with the RC material is mainly attributed to the formation of a larger number of micro-cells (because of the higher number density of cathodic sites) as well as by the less protective film formed on the α-Mg grains (anodic sites) compared to the RC AM50, compare SEM micrographs of the corroded RC and HPDC alloys at 4°C in Fig. 7 and the schematic illustrations in Fig. 11a with Fig. 11b.

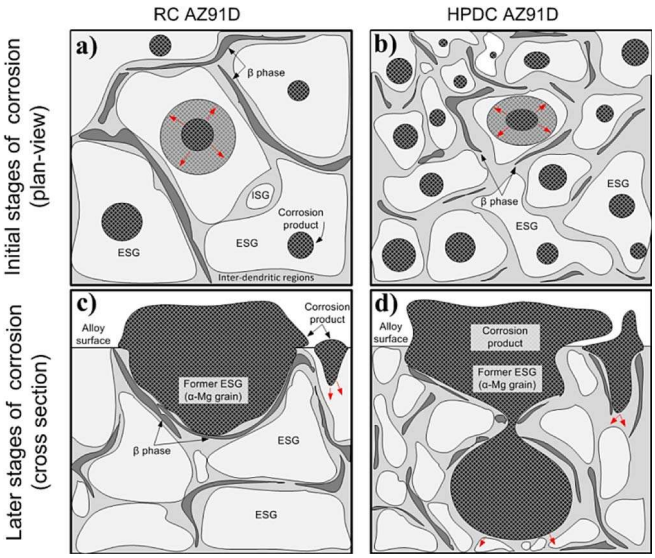

Figure 11. Schematic illustration of the NaCl induced atmospheric corrosion of alloy AZ91D produced by RC (a and c) and HPDC (b and d) techniques during early stages and after long exposure times. Note: the arrows indicate the growth direction of the corrosion pits.

During later stages of corrosion, (in our case > 504 h) the β phase barrier effect becomes pronounced in the RC material. This limits the advance of the corrosion attack and is suggested to be the main reason behind the superior corrosion resistance of the RC AZ91D. A similar barrier effect has been reported by Pardo et al.,[83] who examined the corrosion behavior of alloys AZ31, AZ80 and AZ91D in 3.5 wt% NaCl at 25°C. The present results show that in the case of HPDC AZ91D the barrier effect is less prominent and sets in later compared to the RC material, compare the cross sectional images in Figs. 8b and 8c and the schematic images in Figs. 11c and 11d. This is also shown by the gravimetric results in Fig. 6, where the mass gain curves of the RC and HPDC materials start to become convex after 3 and 6 weeks, respectively. The relative ineffectiveness of the barrier effect in HPDC AZ91D compared to the RC alloy is attributed entirely to microstructure, i.e. to the connectivity and area fraction of β phase. Hence, it is argued that the difference in characteristics of intermetallic β phase particles is the essential factor affecting the corrosion of the alloys examined and that the corrosion of the alloy is under cathodic control rather than anodic control.

The role of η phase particles.—The reports in the literature on the role of η particles on the corrosion of Mg-Al alloys are somewhat contradictory. While several authors have reported that the η phase is cathodically active owing to the high potential difference between it and α-Mg,[82,84] Jönsson et al.[85] reported that η phase exhibits only slight cathodic activity in the initial stages of atmospheric corrosion of alloy AZ91, and claimed that it does not play a vital role in the initiation of corrosion. In contrast, a recent paper of Danaie et al.,[84] reported that accumulations of corrosion products tended to form at η inclusions and attributed this to the cathodic activity of these inclusions. Since the current results show that the fraction and distribution of η particles in the HPDC and in the RC material was was about the same, it is concluded that the differences in corrosion behavior are not related to the η phase particles.

The role of casting pores.—Casting pores are expected to have a detrimental effect on the corrosion properties of Mg alloys. The present results show that macro- and micro-porosities are larger and occupy a higher surface fraction in HPDC AZ91D than in the RC material, see Fig. 4d. Esmialy et al.,[40] who investigated the corrosion behavior of alloy AM50 in cyclic wet/dry atmosphere, reported a significant negative effect of porosity on the corrosion behavior of Mg-Al alloys. Thus, the lower fraction of pores may contribute to the superior

corrosion resistance of RC AZ91D in this study. It may be noted that the interaction of water vapor in entrapped gases with Mg has been reported to lead to a high hydrogen content in the base metal. The high hydrogen content was suggested to cause H_2 (g) evolution, contributing to crack formation.[40] Besides, working with corrosion behavior of a pressure die cast Mg alloy AZ91D, Song et al.[86] proposed a number of possible mechanisms responsible for the faster corrosion rate of the pore-rich regions in the solidification microstructure of alloy.

Conclusions

Rheocasting using the RheoMetal process resulted in a significant improvement in the corrosion resistance of the Mg-Al alloy AZ91D compared to the same alloy produced by the conventional HPDC technique. The improved corrosion properties of the RC alloy was evidenced at 4 and 22°C and were related to microstructural changes due to the special solidification conditions in rheocasting. The main conclusions drawn from this paper are as follows;

1. RC AZ91D exhibited a coarser microstructure than HPDC AZ91D. Thus, the α-Mg grains were larger and frequently appeared as ESGs in the microstructure of the RC material which also exhibited relatively large intermetallic β-phase particles. The microstructure of the HPDC material exhibited finer α-Mg grains and finer and more dispersed β-phase particles. Especially, the degree of connectivity in the β-phase was higher in the microstructure of the RC alloy than in the HPDC alloy. Quantitative image analysis showed that the RC material had a lower fraction of casting defects than the HPDC material.
2. The superior corrosion resistance of RC AZ91D compared to HPDC AZ91D at the temperatures studied is attributed to microstructural differences between the materials. Initially, the larger number density of cathodic β-phase particles in the HPDC material causes faster corrosion compared to the RC material. During later stages of corrosion, the network-like β-phase particles in the RC alloy act as a corrosion barrier, further improving the relative corrosion resistance of the RC material. Additionally, a higher Al content in the α-Mg grains of the RC material resulted in a more resistant surface film compared to the HPDC alloy.

Acknowledgments

The funding of this research by the Swedish foundation for strategic research (SSF) is gratefully acknowledged. The authors would also like to thank Husqvarna AB for providing the HPDC AZ91D materials.

References

1. C. F. Li, M. J. Wang, W. H. Ho, H. N. Li, and S. K. Yen, *J. Electrochem. Soc.*, **158**, C11 (2011).
2. M. Jonsson, D. Persson, and R. Gubner, *J. Electrochem. Soc.*, **154**, C684 (2007).
3. U. M. Tefashe, M. E. Snowden, P. Ducharme Dauphin, M. Danaie, G. A. Botton, and J. Mauzeroll, *J. Electroanal. Chem.* **720–721**, 121 (2014).
4. J. E. Gray and B. Luan, *J. Alloy. Compd.*, **336**, 88 (2002).
5. J. R. Kish, Y. Hu, J. Li, and J. R. McDermid, *Corrosion*, **68**, 468 (2010).
6. J. H. Nordlien, K. Nisancioglu, S. Ono, and N. Masuko, *J. Electrochem. Soc.*, **144**, 461 (1997).
7. J. H. Nordlien, K. Nisancioglu, S. Ono, and N. Masuko, *J. Electrochem. Soc.*, **143**, 2564 (1996).
8. J. H. Nordlien, S. Ono, N. Masuko, and K. Nisancioglu, *J. Electrochem. Soc.*, **142**, 3320 (1995).
9. Y. H. Huang, Y. L. Lee, and C. S. Lin, *J. Electrochem. Soc.*, **158**, C310 (2012).
10. K. Huber, *J. Electrochem. Soc.*, **100**, 376 (1953).
11. P. Zoltowski, *J. Electroanal. Chem.*, **443**, 149 (1998).
12. S. V. Lamak, H. B. Xue, N. N. A. H. Meis, A. C. C. Esteves, and M. G. S. Ferreira, *Prog. Organ. Coat.*, **80**, 98 (2015).
13. Z. Cheng, J. Lian, Y. Hui, and G. Li, *J. Bionic Eng.*, **11**, 610 (2014).
14. C. Wang, B. Jiang, M. Liu, and Y. Ge, *J. Alloy. Comp.*, **621**, 53 (2015).
15. S. V. Lamak, H. B. Xue, N. N. A. H. Meis, A. C. C. Esteves, and M. G. S. Ferreira, *Prog. Organ. Coat.*, **80**, 98 (2015).
16. O. Lunder, T. Kr Aune, and K. Nisancioglu, *Corrosion*, **43**, 291 (1987).
17. X. Yue and L. Sha, *J. Rare Earths*, **25**, 201 (2007).
18. G. Pettersen, H. Westengen, R. Høier, and O. Lohne, *Mater. Sci. Eng. A*, **15**, 115 (1996).
19. H. J. Zhang, D. F. Zhang, C. H. Ma, and S. F. Guo, *Mater. Lett.*, **92**, 45 (2013).
20. P. Kapranos, D. Brabazon, S. P. Midson, S. Naher, and T. Haga, *Comp. Mater. Proc.*, **5**, 3 (2014).
21. M. M. Advedesian and H. Baker, Magnesium and magnesium alloys, *ASM Specialty Handbook*, ASM International, Materials Park (1999).
22. M. Siedersleben, *Vakuum-Druckguss von Magnesiumlegierungen fur hochbelastete Bauteile, Magnesium Eigenschaften*, Wiley-VCH, Weinheim (2000).
23. E. F. Emley, *Principals of magnesium technology*, Pergamon Press, Oxford (1966).
24. Z. Fan, *Int. Mater. Rev.*, **47**, 49 (2002).
25. Z. Koren, H. Rosenson, E. M. Gutman, Y. B. Unigovski, and A. Eliezer, *J. Light. Met.*, **2**, 81 (2002).
26. M. Östklint, M. Wessén, and A. E. W. Jarfors, *Int. J. Cast Metal. Res.* **27**, 235 (2014).
27. M. Östklint, M. Wessén, and A. E. W. Jarfors, *Int. J. Cast Metal. Res.* **28**, 65 (2015).
28. M. Jönsson, D. Thierry, and N. LeBozec, *Corros. Sci.*, **48**, 1193 (2006).
29. L. Yang, Y. Li, Y. Wei, L. Hou, and Y. Tian, *Corros. Sci.*, **52**, 2188 (2010).
30. M. Jönsson, D. Persson, and R. Gubner, *J. Electrochem. Soc.* **154**, C684 (2007).
31. Z. Cui, X. Li, K. Xiao, and C. Dong, *Corros. Sci.*, **76**, 243 (2013).
32. R. Lindström, J. E. Svensson, and L. G. Johansson, *J. Electrochem. Soc.*, **149**, B103 (2002).
33. D. B. Blücher, J. E. Svensson, and L. G. Johansson, *J. Electrochem. Soc.*, **150**, B93 (2003).
34. M. Esmaily, M. Shahabi-Navid, J. E. Svensson, M. Halvarsson, L. Nyborg, Y. Cao, and L. G. Johansson, *Corros. Sci.*, **90**, 420 (2014).
35. D. B. Blücher, J. E. Svensson, L. G. Johansson, M. Rohwerder, and M. Stratmann, *J. Electrochem. Soc.*, **151**, B621 (2004).
36. M. Esmaily, N. Mortazavi, M. Shahabi-Navid, J. E. Svensson, M. Halvarsson, L. Nyborg, Y. Cao, and L. G. Johansson, *J. Electrochem. Soc.*, **162**, C85 (2014).
37. S. Mathieu, C. Rapin, J. Hazan, and P. Steinmetz, *Corros. Sci.* **44**, 2737 (2002).
38. B. Mingo, R. Arrabal, M. Mohedano, A. Pardo, E. Matykina, and A. Rivasc, *J. Electrochem. Soc.*, **162**, C180 (2015).
39. M. Esmaily, M. Shahabi-Navid, N. Mortazavi, J. E. Svensson, M. Halvarsson, M. Wessén, A. E. W. Jarfors, and L. G. Johansson, *Mater. Charac.*, **95**, 50 (2014).
40. M. Esmaily, M. Strom, J. E. Svensson, M. Halvarsson, and L. G. Johansson, *Corrosion* In press (2015).
41. T. E. Graedel, *J. Electrochem. Soc.*, **136**, 204 (1989).
42. P. V. Strekalov, *Prot. Met.*, **29**, 673 (1993).
43. M. Repoux, *Surf. Inter. Anal.*, **18**, 567 (1992).
44. A. K. S. Bankoti, A. K. Mondal, S. Kumar, and B. C. Ray, *Mater. Sci. Eng. A*, **626**, 186 (2015).
45. S. Luo, Q. Chen, and Z. Zhao, *J. Alloy. Comp.*, **477**, 602 (2009).
46. R. M. Wang, A. Eliezer, and E. M. Gutman, *Mater. Sci. Eng. A*, **355**, 201 (2003).
47. Y. Ma, J. Zhang, and M. Yang, *J. Alloy. Comp.*, **470**, 515 (2009).
48. F. Czerwinski, *Acta Mater.*, **50**, 2639 (2002).
49. A. H. Feng and Z. Y. Ma, *Scripta Mater.*, **56**, 397 (2007).
50. S. Celotto and T. J. Bastow, *Acta Mater.* **49**, 41 (2001).
51. S. Schumann and H. Friedrich, Engineering requirements, strategies and examples, in: H. E. Friedrich and B. L. Mordike (Eds.), *Magnesium Technology, Applications*, Springer-Verlag, Berlin, Germany (2006).
52. S. N. Mathaudhu, W. H. Sillekens, N. R. Neelameggham, and N. Hort, *Magnesium Technology 2012*, The Minerals, Metals, & Materials Society (2012).
53. M. Sumida, S. Jung, and T. Okane, *Mater. Trans.*, **50**, 1161 (2009).
54. M. Danaie, R. M. Asmussen, P. Jakupi, W. D. Shoesmith, and G. A. Botton, *Corros. Sci.*, **77**, 151 (2013).
55. X. Zheng, A. Luo, C. Zhang, J. Dong, and R. Waldo, *Metall. Mater. Trans. A*, **43**, 3239 (2012).
56. D. Mirković and R. Schmid-Fetzer, *Metall. Mater. Trans. A*, **40**, 974 (2009).
57. D. Mirković and R. Schmid-Fetzer, *Metall. Mater. Trans. A*, **40**, 958 (2009).
58. A. L. Bowles, T. J. Bastow, C. J. Davidson, J. R. Griffiths, and P. D. D. Rodrigo, *Magnesium Technology*, The Minerals Metals and Materials Society, Nashville, USA (2000).
59. Z. Z. G. Fan Liu and Y. Wang, *J. Mater. Sci.*, **41**, 3631 (2006).
60. J. Zhang, X. Niu, X. Qiu, K. Liu, C. Nan, D. Tang, and J. Meng, *J. Alloy. Comp.*, **471**, 322 (2009).
61. L. Bichler, K. Lee, A. Elsayed, and C. Ravindran, *Int. J. Metalcasting*, **1**, 43 (2008).
62. M. R. Barone and D. A. Caulk, *Int. J. Eng. Sci.*, **38**, 1279 (2000).
63. M. J. Blandamer, J. B. F. Engberts, P. T. Glesson, and J. R. Reis, *Chem. Soc. Rev.*, **34**, 440 (2005).
64. G. L. Song and A. Atrens, *Adv. Eng. Mater.* **1**, 11 (1999).
65. G. L. Song and A. Atrens, *Adv. Eng. Mater.*, **9**, 177 (2007).
66. G. L. Song, *Adv. Eng. Mater.* **7**, 563 (2005).
67. G. S. Frankel, A. Samaniego, and N. Birbilis, *Corros. Sci.*, **70**, 104 (2013).
68. S. Thomas, N. V. Medhekar, G. S. Frankel, and N. Birbilis, *Curr. Opin. Solid State Mater. Sci.*, **19**, 85 (2015).
69. D. Thirumalaikumarasamy, K. Shanmugam, and V. Balasubramanian, *J. Magnes. Alloy.*, **2**, 36 (2014).
70. G. Baril and N. Pebere, *Corros. Sci.*, **43**, 471 (2001).
71. G. S. Frankel and N. Sridhar, *Mater. Today*, **11**, 38 (2008).
72. G. S. Frankel, *J. Electrochem. Soc.*, **145**, 2186 (1998).
73. M. Shahabi-Navid, M. Esmaily, J. E. Svensson, M. Halvarsson, L. Nyborg, Y. Cao, and L. G. Johansson, *J. Electrochem. Soc.*, **161**, C277 (2014).
74. D. A. Vermilyea and C. F. Kirk, *J. Electrochem. Soc.*, **116**, 1487 (1969).
75. P. F. King, *J. Electrochem. Soc.*, **110**, 1113 (1963).
76. C. F. Li, W. H. Ho, and S. K. Yen, *J. Electrochem. Soc.*, **156**, E29 (2009).

77. M. Taheri and J. R. Kish, *J. Electrochem. Soc.*, **160**, C36 (2013).
78. T. Ramgopal, P. Schmutz, and G. S. Frankel, *J. Electrochem. Soc.*, **148**, B348 (2001).
79. D. Daloz, P. Steinmetz, and G. Michot, *Corros. Sci.*, **53**, 944 (1997).
80. G. Song, A. Atrens, and M. Dargusch, *Corros. Sci.*, **41**, 249 (1998).
81. R. M. Asmussen, W. J. Binns, P. Jakupi, and D. W. Shoesmith, *J. Electrochem. Soc.*, **161**, C501 (2014).
82. O. Lunder, J. E. Lein, T. Kr Aune, and K. Nisancioglu, *Corrosion*, **45**, 741 (1989).
83. A. Pardo, M. C. Merino, A. E. Coy, R. Arrabal, F. Viejo, and E. Matykina, *Corros. Sci.*, **50**, 823 (2008).
84. M. Danaie, R. M. Asmussen, P. Jakupia, D. W. Shoesmith, and G. A. Botton, *Corros. Sci.*, **83**, 299 (2014).
85. M. Jönsson, D. Persson, and D. Thierry, *Corros. Sci*, **49**, 1540 (2007).
86. G. L. Song, D. H. St John, and T. Abbott, *Int. J. Cast Metal. Res.*, **18**, 174 (2005).